The Astrophysical Journal, 893:83 (15pp), 2020 April 10 https://doi.org/10.3847/1538-4357/ab7fa6

Assessment of Critical Convection and Associated Rotation States in Models of Sun-like Stars Including a Stable Layer

Shin-ichi Takehiro[1], Allan Sacha Brun[2], and Michio Yamada[1]
[1] RIMS, Kyoto University, Japan; takepiro@gfd-dennou.org
[2] DAp/AIM, CEA Paris-Saclay, CNRS/INSU, Univ. of Paris 7, France
Received 2019 December 19; revised 2020 March 6; accepted 2020 March 9; published 2020 April 17

Abstract

Recent numerical simulations of rotating stellar convection have suggested the possible existence of retrograde (slow equator, fast poles) or so-called antisolar differential rotation states in slowly rotating stars possessing a large Rossby number. We aim to understand whether such rotational states exist from the onset of convective instability or are the outcome of complex nonlinear interactions in the turbulent convective envelope. To this end, we have made a systematic linear analysis of the critical state of convection in a series of 15 numerical simulations published in Brun et al. We have assessed their degree of supercriticality and most-unstable mode properties, and computed the second-order mean zonal flow response. We find that none of the linear critical cases show a retrograde state at the onset of convection even when their nonlinear counterparts do. We also find that the presence of a stably stratified layer coupled to the convectively unstable upper layer leads to interesting gravity-wave excitation and angular momentum transport. We conclude that retrograde states of differential rotation are probably the outcome of complex mode–mode interactions in the turbulent convection layer and are, as a consequence, likely to exist in real stars.

Unified Astronomy Thesaurus concepts: Stellar convective zones (301); Stellar interiors (1606); Astrophysical fluid dynamics (101); Internal waves (819); Stellar rotation (1629)

1. Introduction

Stars can play the role of a modern physics laboratory, because processes as diverse as turbulence, thermal convection, plasma eruption, magnetic flux emergence, magnetic reconnection, and rotation-induced large-scale mean flows can be studied in detail via direct surface observations (or indirectly via asteroseismology) allowing their complex dynamics to be characterized with an ever improving accuracy. Of fundamental interest is turbulent convection, because it is both at the source of many of the most dynamical phenomena observed in stars and it impacts directly their short- and long-term evolution. Turbulent convection in stellar envelope helps transport the heat generated deep inside their nuclear core. Depending on their mass M_*, high- or low-mass stars (with respect to the reference solar value $M_\odot$) have different internal structures, and convection zones are not found at the same location. In massive stars ($M_* > 2M_\odot$), convection is mostly confined in the deep interior, in the so-called core convection region, with little stratification. By contrast, solar-type stars and stars less massive than the Sun have their convective zone located near their surface. This convective envelope deepens as the star becomes less and less massive, eventually occupying the whole star below 0.3 $M_\odot$. This deepening of the convective envelope is accompanied by increasingly stronger stratification. Hence, the convective process in stars experiences a large range of conditions, and it needs to be studied in detail to understand how it is modified under these changing situations. Moreover, stars are rotating objects. Turbulent convection motions are thus influenced by the action of the Coriolis force and in the most extreme rotating situation, the star and all its internal layers (convective and radiative) are even deformed by the centrifugal force, losing their spherical shape (Wang et al. 2016; Zorec et al. 2017). So, rotating convection zones not only transport heat and energy but also angular momentum, yielding large-scale mean flows such as differential rotation and meridional circulation (Brun & Rempel 2009). A well-known, nondimensional number, the Rossby number *Ro*,[3] is being used to characterize the influence of rotation on convective motions (Landin et al. 2010; Brun et al. 2017; Amard et al. 2019). For small *Ro*, rotational effects are large, and convective motions feel the Coriolis force and adapt themselves accordingly by being tilted with respect to the local vertical direction. By contrast for large *Ro*, rotational effects are small, leading to classical nonrotating slab convection behavior (purely up and down motions). In the present study, we aim to characterize stellar convection and its associated large-scale mean flows in solar-like stars by means of 3D numerical simulations of convection in a spherical shell for varying Rossby numbers. More specifically, we wish to understand how the basic state of convection and the associated mean flows at the onset of convective instability are behaving compared to their nonlinear counterpart, such as the ones published in Brun et al. (2017). One key result of the numerical simulation of rotating convection in a spherical shell has been to propose the possible existence of a retrograde state of differential rotation with a slow equator and fast poles for slowly rotating stars with a large Rossby number (Matt et al. 2011; Guerrero et al. 2013; Gastine et al. 2014; Karak et al. 2015; Brun et al. 2017; Viviani et al. 2019). This so-called antisolar rotation state, in reference to the Sun's prograde differential rotation that instead possesses a fast equator and slow poles, is very interesting because it can influence the evolution and dynamics of these stars via, for instance, a modification of their dynamo and magnetism and

[3] This number has many definitions in the literature. In this paper, we use the fluid one, i.e., that comparing the Coriolis force to the advection term in the Navier–Stokes equation (e.g., $R_o = \tilde{\omega}/2\Omega_*$, with $\tilde{\omega}$ the rms vorticity and Ω_* the stellar rotation rate), as it is the most meaningful when studying 3D nonlinear convective numerical simulations.

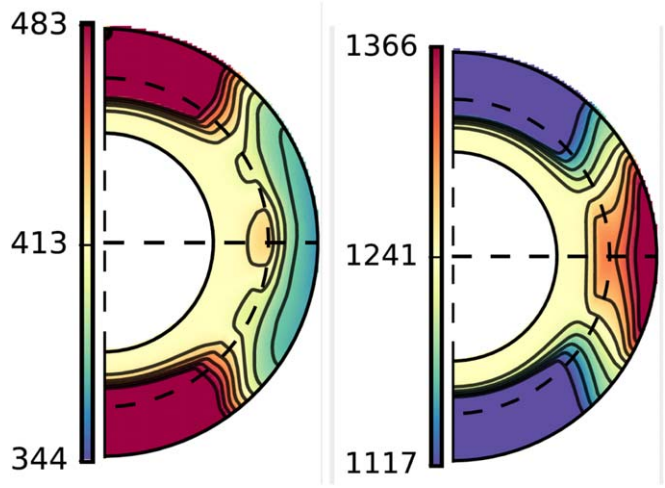

Figure 1. Differential rotation profiles in a solar-like star: comparing antisolar (left) to solar-like (right) cases. Contour plots in meridional cuts of angular velocity with red tones indicating prograde flows (Brun et al. 2017).

the associated stellar wind dynamics and the rotational braking it involves (Réville et al. 2015; Vidotto et al. 2016). Moreover, we could also wonder how dynamo action and cycles could be affected by the antisolar Ω effect (Strugarek et al. 2018; Viviani et al. 2019; Karak et al. 2020).

We illustrate an example of such retrograde and prograde states of differential rotation in Figure 1. In this study, we wish to understand whether retrograde states of rotation as shown in the left panel of Figure 1 are robust and naturally present in the convective flow at the onset of the instability or instead the outcome of nonlinear processes. To this aim, we have systematically computed the critical state at the onset of convection instability for the 15 simulations of rotating stellar convection published in Brun et al. (2017) and assessed the second-order mean flows of each marginal states. Such approaches have already been done in the context of Boussinesq convection in the planetary convection setup (see, for instance, Takehiro & Hayashi 1999; Dormy et al. 2004, and references therein) and only recently extended to the anelastic approaches which are essential to take into account when considering solar-like stars with highly stratified outer convective envelope (Jones et al. 2009; Sasaki et al. 2018). They of course follow a long history of such studies first started by Chandrasekhar in the 1960's (Chandrasekhar 1961), soon followed by Roberts, Busse and Gilman few years later (Roberts 1968; Busse 1970; Gilman 1975, 1977). These studies have shown some interesting trends with key control parameters such as the Ekman E_k or Taylor Ta numbers (a measure of rotational effect with respect to viscous ones; $E_k = 2/\sqrt{Ta}$), the number of density scale heights N_ρ across the convective domain, the aspect ratio β, or the Prandtl number (measuring the relative importance of viscous versus thermal effects), to cite only a few. For instance, it is common knowledge that convection is harder to trigger with increasing rotational constraint. The critical Rayleigh number Ra_c, frequency ω_c, and azimuthal wavenumber m_c are found to scale respectively with $E_k^{-4/3}$, $E_k^{-2/3}$, and $E_k^{-1/3}$. Higher density scale height or slender convective layers also tend to make Ra_c, ω_c, and m_c larger (see Jones et al. 2009 for more details and the sections below). The difference between anelastic and Boussinesq linear stability analysis rests more, for instance, in the values of the critical parameters, often much higher in the anelastic stratified case than in the scaling with E_k, which is roughly similar. Moreover, the location of the most-unstable mode in highly stratified layers tends to be closer to the top of the domain and of much smaller spatial scale. Also note that in Takehiro & Hayashi (1999), retrograde states have already been found. The regime diagrams published in this study have been shown to be quite complex in some area of the parameter space involving β, E_k, and Pr, with retrograde mean flows only found in some very specific cases when Pr is large. Further, these retrograde states, assuming there is no Reynolds stress, are the consequence of viscous diffusion playing a key role as a response to the angular momentum transport by the thermal contribution (part) of the meridional circulation due to the $v \cdot \nabla S$ term in the heat equation (see Equation (3) below). In stars, however, atomic Prandtl numbers are very small, of order 10^{-5} or less and so these retrograde states are unlikely, and the simulations published in Brun et al. (2017) all have $Pr = 0.25$. So, the retrograde state found in the nonlinear solutions are supposedly not in the same parameter area as those required to find the balance between thermal advection and viscous diffusion, but we will of course verify that hypothesis in this work.

Hence, the analysis presented in this paper is the continuation of these previous convection stability studies (the most recent ones considering anelastic approximation) but focus on stars and add one more important ingredient: an inner stably stratified radiative zone. As we will see, this has interesting consequences because the bottom boundary condition of the stability analysis differs significantly from an impenetrable wall and internal gravity waves can even be excited in that layer. Another key difference is the fact that stars have a well-defined luminosity $L_* = 4\pi R_*^2 \sigma T_{\rm eff}^4$, with R_* the star radius, σ the Stefan constant, and $T_{\rm eff}$ the surface effective temperature (equal to 5800 K for the Sun, for instance). Hence, our regime diagram study will be made by fixing the luminosity of the various model solar-type stars we are considering (see below for more details). Often in geophysics studies luminosity constraint is relaxed. Finally, along with the inclusion of an inner stably stratified layer, we will also consider the role of radiative flux in the stability analysis. For the same reason that we just discussed, this has never been considered in previous studies mostly concerned with planetary flows.

In the next section, we present the governing equations and the 15 star models we have considered. Then in Section 3, the principles we followed to perform the stability analysis are discussed. In Section 4 we present our results on the critical Rayleigh number Ra_c, frequency ω_c, and azimuthal wavenumber m_c. We illustrate the various marginal state solutions. In Section 5, we derive the equations used to compute the second-order mean flow and present the resulting differential rotation mean flows, including the possibility that gravity waves help transport angular momentum in the stable layer in some high Ekman number solutions. Finally, we conclude in Section 6.

2. Governing Equations

The system is described by the equations for anelastic fluid (e.g., Jones et al. 2011) where the term for temperature diffusion is added to the energy equation and a stable layer below the

convective envelope is taken into account (e.g., Brun et al. 2011),

$$\nabla \cdot (\overline{\rho}\boldsymbol{u}) = 0, \tag{1}$$

$$\frac{\partial \boldsymbol{u}}{\partial t} - \boldsymbol{u} \times \boldsymbol{\omega} + 2\Omega \boldsymbol{k} \times \boldsymbol{u} = -\nabla \Pi - \frac{S}{C_p}\boldsymbol{g}(r) + \frac{1}{\overline{\rho}}\boldsymbol{F}_\nu, \tag{2}$$

$$\begin{aligned}
&\Pi = \frac{p}{\overline{\rho}} + \frac{1}{2}|\boldsymbol{u}|^2,\\
&(\boldsymbol{F}_\nu)_i = \frac{\partial}{\partial x_j}\left\{\overline{\rho}\nu\left(\frac{\partial u_i}{\partial x_j} + \frac{\partial u_j}{\partial x_i} - \frac{2}{3}\delta_{ij}\frac{\partial u_k}{\partial x_k}\right)\right\},\\
&\overline{\rho}\overline{T}\left[\frac{\partial S}{\partial t} + (\boldsymbol{u}\cdot\nabla)(\overline{S}+S)\right]\\
&\quad = \nabla\cdot[\kappa_{\rm rad}\overline{\rho}C_p\nabla(\overline{T}+T) + \kappa\overline{\rho}\overline{T}\nabla S + \kappa_0\overline{\rho}\overline{T}\nabla\overline{S}] + \overline{\rho}\epsilon + Q_\nu,\\
&Q_\nu = \frac{\overline{\rho}\nu}{2}\left(\frac{\partial u_i}{\partial x_j} + \frac{\partial u_j}{\partial x_i} - \frac{2}{3}\delta_{ij}\frac{\partial u_k}{\partial x_k}\right)^2,
\end{aligned} \tag{3}$$

where $\boldsymbol{u}$ is velocity, $\boldsymbol{\omega} = \nabla \times \boldsymbol{u}$ is vorticity, and ρ, p, S, and T are density, pressure, entropy, and temperature, respectively. $\overline{\cdot}$ indicates that the variable is for the basic state of the anelastic system. The physical constants appearing in the equations are the specific heat at constant pressure C_p, angular velocity of the system Ω. The kinematic viscosity ν, thermal diffusivity κ, thermal diffusivity for the horizontally homogeneous component κ_0, and radiation thermal diffusivity $\kappa_{\rm rad}$ are given as functions of the radius r only. ϵ is the body-heating term by nuclear reactions and is expressed as $\epsilon = \epsilon_0\overline{T}^n$, where n is adjusted to best reproduce the 1D stellar model profile. The coefficient ϵ_0 must satisfy $\int dS\int_0^{r_o}\epsilon\, r^2 dr = \mathcal{L}$, where $\mathcal{L}$ is the luminosity of the star.

The diffusion coefficient of the entropy gradient term on the right-hand side of the energy Equation (3) is changed from κ to κ_0 for the spherically homogeneous component of S:

$$\kappa\overline{\rho}\overline{T}\nabla S \to \begin{cases}\kappa_0\overline{\rho}\overline{T}\nabla S_0 & \text{for spherically homogeneous component of } S\,.\\ \kappa\overline{\rho}\overline{T}\nabla S & \text{others}\end{cases} \tag{4}$$

The boundary conditions for the velocity field we consider are

$$u_r = \sigma_{r\phi} = \sigma_{r\theta} = 0, \tag{5}$$

where u_r is the radial component of velocity, and σ_{ij} is the stress tensor. The thermal boundary condition is the fixed-energy flux condition:

$$\kappa_{\rm rad}\overline{\rho}C_p\nabla(\overline{T}+T) + \kappa\overline{\rho}\overline{T}\nabla S + \kappa_0\overline{\rho}\overline{T}\nabla\overline{S} = \text{const. at } r = r_i,\ r_0. \tag{6}$$

In contrast, Brun et al. (2011, 2017) use the fixed radial gradient of the entropy condition, which does not fix the energy flux at the boundary exactly. However, this condition approximately gives the fixed-energy flux condition owing to the values of $\kappa_{\rm rad}$, and κ_0, κ. Near the outer boundary, they give the thermal diffusivities satisfying $\kappa_{\rm rad} \ll \kappa_0$, κ. Then, the radiative energy flux can be ignored, and entropy diffusion only contributes to the energy flux. Therefore, when the radial entropy gradient is fixed, the energy flux is approximately fixed at the outer boundary. On the other hand, at the inner boundary, the fixed-energy flux condition is necessarily satisfied. But when (statistically) steady state is obtained, the energy flux at the inner boundary is fixed at a certain value depending on the energy flux at the outer boundary. Here, considering a comparison with Brun et al. (2015, 2017), we use the fixed radial entropy gradient condition:

$$\frac{\partial}{\partial r}(\overline{S} + S) = \text{const. at } r = r_i,\ r_0. \tag{7}$$

A thermodynamic relation is needed to close the system. We consider here an ideal gas; however, we do not use the equation of state $p = \rho RT$ directly, but the linearized equation with respect to the basic state of the anelastic approximation:

$$\frac{\rho}{\overline{\rho}} = \frac{p}{\overline{p}} - \frac{T}{\overline{T}} = \frac{p}{\gamma\overline{p}} - \frac{S}{C_p}, \tag{8}$$

where γ is the adiabatic index, C_P the specific heat capacity, and R the gas constant. The relation between C_p and R is given by $R = C_p(1 - 1/\gamma)$.

3. Linear Stability Analysis

In order to perform linear stability analysis, the governing equations are linearized with respect to the background state as follows:

$$\nabla \cdot (\overline{\rho}\boldsymbol{u}') = 0, \tag{9}$$

$$\frac{\partial \boldsymbol{u}'}{\partial t} + 2\Omega\boldsymbol{k} \times \boldsymbol{u}' = -\nabla\left(\frac{p'}{\overline{\rho}}\right) + \frac{S'}{C_p}\boldsymbol{g}(r) + \frac{1}{\overline{\rho}}\boldsymbol{\mathcal{F}}'_\nu, \tag{10}$$

$$\begin{aligned}
&(\mathcal{F}'_\nu)_i = \frac{\partial}{\partial x_j}\left\{\overline{\rho}\nu\left(\frac{\partial u_i'}{\partial x_j} + \frac{\partial u_j'}{\partial x_i} - \frac{2}{3}\delta_{ij}\frac{\partial u_k'}{\partial x_k}\right)\right\},\\
&\overline{\rho}\overline{T}\left[\frac{\partial S'}{\partial t} + u_r'\frac{d}{dr}(\overline{S} + S_0)\right] = \nabla\cdot[\kappa_{\rm rad}\overline{\rho}C_p\nabla T' + \kappa\overline{\rho}\overline{T}\nabla S'],
\end{aligned} \tag{11}$$

where $(\cdot)'$ expresses disturbance variables. $\overline{S}(r) + S_0(r)$ is the entropy profile of the basic state, where S_0 is the solution of the following diffusive equation and the hydrostatic equation:

$$0 = -\frac{d}{dr}\left(\frac{p_0}{\overline{\rho}}\right) + \frac{S_0}{C_p}g(r), \tag{12}$$

$$\begin{aligned}
0 = \frac{1}{r^2}\frac{d}{dr}r^2\Bigg[&\kappa_{\rm rad}\overline{\rho}C_p\frac{d}{dr}(\overline{T} + T_0)\\
&+ \kappa_0\overline{\rho}\overline{T}\frac{d\overline{S}}{dr} + \kappa_0\overline{\rho}\overline{T}\frac{dS_0}{dr}\Bigg].
\end{aligned} \tag{13}$$

Here, $(\cdot)_0$ means a horizontally homogeneous variable. We ignore the nuclear heating term because its effect on the basic entropy gradient profile is negligible.

We assume that each disturbance variable is in proportion to $\exp(\sigma t)$. $\sigma = \sigma_r + i\sigma_i$ is a complex number, whose real and imaginary parts are the growth rate and frequency, respectively. Because the basic state depends only on r, spherical harmonic expansion is applied to the disturbance equations. Further, Chebyshev polynomials are used to express radial profiles. Then, an eigenvalue problem of the coefficients with spherical

Table 1
The Rayleigh and Ekman Numbers for the Nonlinear Calculations

	L	$g^{(c)}$	$dS^{*(p)}/dr$	$\kappa^{*(c)}$	$\nu^{*(c)}$	Ω^*	Ra^*	Ek^*
M05S	1.3e10	1.1e5	1.1e−7	1.2e12	3e11	3.25e−7	2.7e6	5.5e−3
M05R1			1.1e−7	5e11	1.25e11	2.6e−6	1.6e7	2.8e−4
M05R3			2e−7	2.8e11	7e10	7.8e−6	9.2e7	5.3e−5
M05R5			3.1e−7	2e11	5e10	1.3e−5	2.8e8	2.3e−5
M07S	1.3e10	6.5e4	3.5e−7	5e12	1.25e12	7.8e−7	3e5	9.5e−3
M07R1			3.5e−7	3e12	7.5e11	2.6e−6	8.3e5	1.7e−3
M07R3			4.5e−7	1.6e12	4e11	7.8e−6	3.7e6	3e−4
M07R5			4.5e−7	1.5e12	3.75e11	1.3e−5	4.2e6	1.7e−4
M09S	1.6e10	5e4	4e−6	1e13	2.5e12	1.3e−6	1.5e6	7.5e−3
M09R1			4e−6	8e12	2e12	2.6e−6	2.3e6	3e−3
M09R3			3.2e−6	5e12	1.25e12	7.8e−6	4.8e6	6.3e−4
M09R5			3.2e−6	4e12	1e12	1.3e−5	7.5e6	3e−4
M11R1	2e10	2.8e4	3e−5	3e13	7.5e12	2.6e−6	1.7e6	7.2e−3
M11R3			2.1e−5	1.6e13	4e12	7.8e−6	4.2e6	1.3e−3
M11R5			2.1e−5	1.2e13	3e12	1.3e−5	7.5e6	5.8e−4

harmonics indices and Chebyshev polynomial order is obtained.

To search for the critical states, we change the amplitude of the thermal diffusivity and viscosity with respect to the disturbance variables, S_0 and T_0, while their profiles are maintained. Moreover, the angular velocity of the star is also magnified to keep the value of the Ekman number. Specifically,

$$\kappa = \kappa^* f,\ \kappa_0 = \kappa_0^* f,\ \kappa_{\rm rad} = \kappa_{\rm rad}^* f,\ \nu = \nu^* f,$$
$$\Omega = \Omega^* f, \tag{14}$$

where the asterisk means the values of the original models. Then, neutral solutions with $\sigma_r = 0$ are searched. Note that we do not change the diffusive coefficients for the background state of the anelastic systems. The merit of this procedure is that the profile of the basic entropy gradient is unchanged, meaning that the thicknesses of the convection and radiation layers do not vary. From diffusion coefficients of the obtained neutral states, we calculate the neutral Rayleigh number as a function of azimuthal wavenumber. The critical azimuthal wavenumber and Rayleigh number are given by the minimum of the neutral Rayleigh number. The standard definition of the Rayleigh number is, for example (Matt et al. 2011),

$$R_{a,\rm trad} = \frac{\left(-\frac{\partial \rho}{\partial S}\right)\Delta S g L^3}{\overline{\rho}\kappa\nu}. \tag{15}$$

Here, the values of each parameter are evaluated at the middle of the convection layer. From Equation (8), $-(1/\overline{\rho})(\partial\rho/\partial S)_p = \frac{1}{C_p}$. However, this Rayleigh number is not suitable to discuss critical states as ΔS is not a control parameter in our setup. We use the following Rayleigh number with the value of the dS/dr of the diffusive solutions:

$$Ra = \frac{g^{(c)}}{C_p}\frac{|dS^{(p)}/dr|L^4}{\kappa^{(c)}\nu^{(c)}}, \quad Ek = \frac{\nu^{(c)}}{\Omega L^2}. \tag{16}$$

Here, $^{(c)}$ indicates the value at the middle of the convective layer, and $^{(p)}$ means the peak value (see Figure 2). L is the thickness of the convective layer.

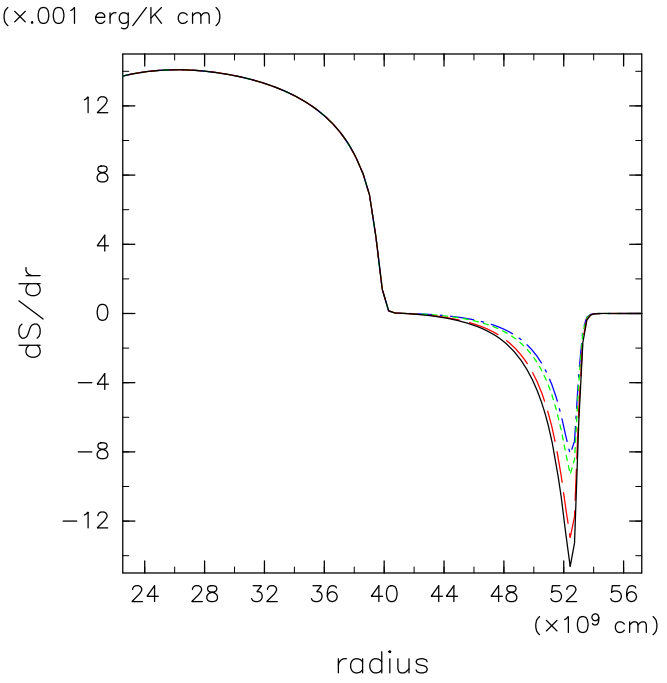

Figure 2. Typical profile of the entropy gradient resulting from our critical state analysis for the case M09 series. We note the deepening of the superadiabatic peak as we increase the rotation rate (lower the Ekman number).

4. Results of Linear Stability Analyses

We now discuss the results of the linear stability analysis of the 15 solar-type star models considered in this study, directly inspired by the nonlinear calculation published in Brun et al. (2017). These models cover a wide range of Ekman numbers, and all have a significant level of stratification. As in Brun et al. (2017), we will follow a simple naming scheme for the models, with first a number indicating the stellar mass in units of the solar mass $M_\odot$ and then a series of letters and numbers indicating the rotation rate of the model. So, for instance, case M05R3 is a numerical simulation intended to model a half-solar-mass star rotating at three times the solar rate. We have also used the letter S when the models are slowly rotating, such that their fluid Rossby number is greater than 1. Key parameters of the models are summarized in Table 1.

Table 2
The Critical Parameters Obtained by Linear Stability Analysis

	m_c	ω_c	f	$dS^{(p)}/dr$	$\kappa^{(c)}$	$\nu^{(c)}$	Ra_c	Ra^*/Ra_c
M05S	8	2.7e−4	1371	1.75e−3	1.4e15	3.5e14	3.2e4	84
M05R1	26	6e−4	753	3.2e−3	4e14	1e14	7.2e5	22
M05R3	47	8.6e−4	558	4.2e−3	1.4e14	3.5e13	7.7e6	12
M05R5	62	1.0e−3	482	5e−3	1e14	2.5e13	1.8e7	16
M07S	10	2.3e−4	495	2e−3	3e15	7.5e14	4.7e3	64
M07R1	21	3.8e−4	372	2.7e−3	1.2e15	3e14	4e4	21
M07R3	37	5.8e−4	284	3.5e−3	5e14	1.25e14	3e5	12
M07R5	48	6.8e−4	247	4e−3	3.2e14	8e13	8.3e5	5.1
M09S	11	3e−4	366	8e−3	4e15	1e15	1.9e4	79
M09R1	16	5.1e−4	321	9e−3	2e15	5e14	8.4e4	27
M09R3	33	7e−4	230	1.2e−2	1e15	2.5e14	4.5e5	11
M09R5	43	8.7e−4	204	1.4e−2	8e14	2e14	8.2e5	9.1
M11R1	15	3e−4	184	1.3e−2	5e15	1.25e15	2.6e4	65
M11R3	29	5.8e−4	141	1.7e−2	2.4e15	6e14	1.5e5	28
M11R5	40	6.5e−4	122	2e−2	1.6e15	4e14	4e5	19

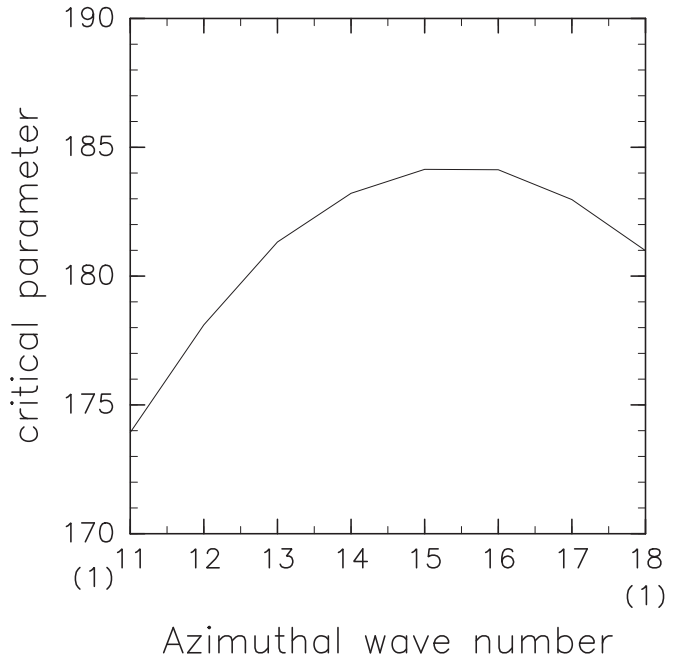

Figure 3. Critical parameter f (magnifying factor of diffusion coefficients) as a function of azimuthal wavenumber for the M11R1 case. This corresponds to the neutral curve in a standard thermal convection problem. The maximum is the critical point ($m_c = 15$).

4.1. Critical Mode and Rayleigh Number

We have performed a systematic analysis of the supercriticality level of the 15 models. By searching for the marginal state of the convection with the method described in Section 3, we were able to assess several key quantities, such as the most critically unstable azimuthal wavenumber m_c, its frequency ω_c, and the corresponding critical Rayleigh number Ra_c.

Figure 3 shows the neutral curve for the M11R1 case, showing the magnifying factor of the diffusion parameter f as a function of azimuthal wavenumber. The maximum of the curve corresponds to the critical state, $m_c = 15$.

We present in Table 2 the outcome of our analysis. For all the cases, we list the critical wavenumber m_c and its frequency ω_c, the factor f that will be used to assess the level of supercriticality, the entropy gradient of the resulting marginal state, and the critical kinematic viscosity and thermal diffusivity. We then assess the critical Rayleigh number Ra_c and compute the level of supercriticality of the nonlinear solution.

We find that the critical modes vary between 8 and up to 62, the largest range of variation being for the M05 case series. This is the consequence of the largest range of Ekman numbers covered by this M05 case series, with the Ekman number varying by more than two decades. Likewise, we see that the critical Rayleigh number Ra_c varies a lot, going from as low as 4.7e3 to as high as 1.8e7, so a more than three order of magnitude change. Again, this is the M05 case series for which this critical parameter varies the most. This is in good quantitative agreement with Jones et al.'s (2009) results, which show very steep variations of Ra_c in their study, leading to a very high value of Ra_c for the onset of convection in rapidly rotating, highly stratified cases. In the three other series, the maximum Ra_c is not as high but does reach a value larger than 10^5. By contrast, we see that the critical frequency ω_c varies by a few, with the lowest value being 2.3×10^{-4} and the highest one 10^{-3}.

Having assessed Ra_c, we can now compute the degree of supercriticality Ra^*/Ra_c of the nonlinear models published in Brun et al. (2017). We see that usually the slowly rotating cases are the most supercritical, with supercritical values between 64 and 84. This is to be expected given the fact that it is hard numerically speaking to maintain the supercriticality level as we increase the rotation rate (or decrease Ek), because at fixed luminosity, this implies having the kinematic viscosity ν and the thermal diffusivity κ scaling like Ω_*^{-2}. As the models span more than a decade in rotation rate, this would imply dropping ν and κ by more than a factor of 100 in the M05 series for instance; this would require very high resolution and large time allocation for such a large parameter study. Instead, the choice was made in Brun et al. (2017) to scale ν and κ as $\Omega_*^{-1/2}$ as a compromise between maintaining a reasonable level of supercriticality while optimizing the computing resources. We see that indeed the faster R5 cases are still supercritical, with values raging from 5.1 to 19.

In Figure 2, we represent the entropy gradient resulting from the linear stability analysis for the M09 case series. We notice the existence of a large negative depth near the surface of the model, which reaches an amplitude (in absolute sense) similar to that of the stably stratified layer. This is much larger that the entropy gradient observed in the nonlinear cases published in

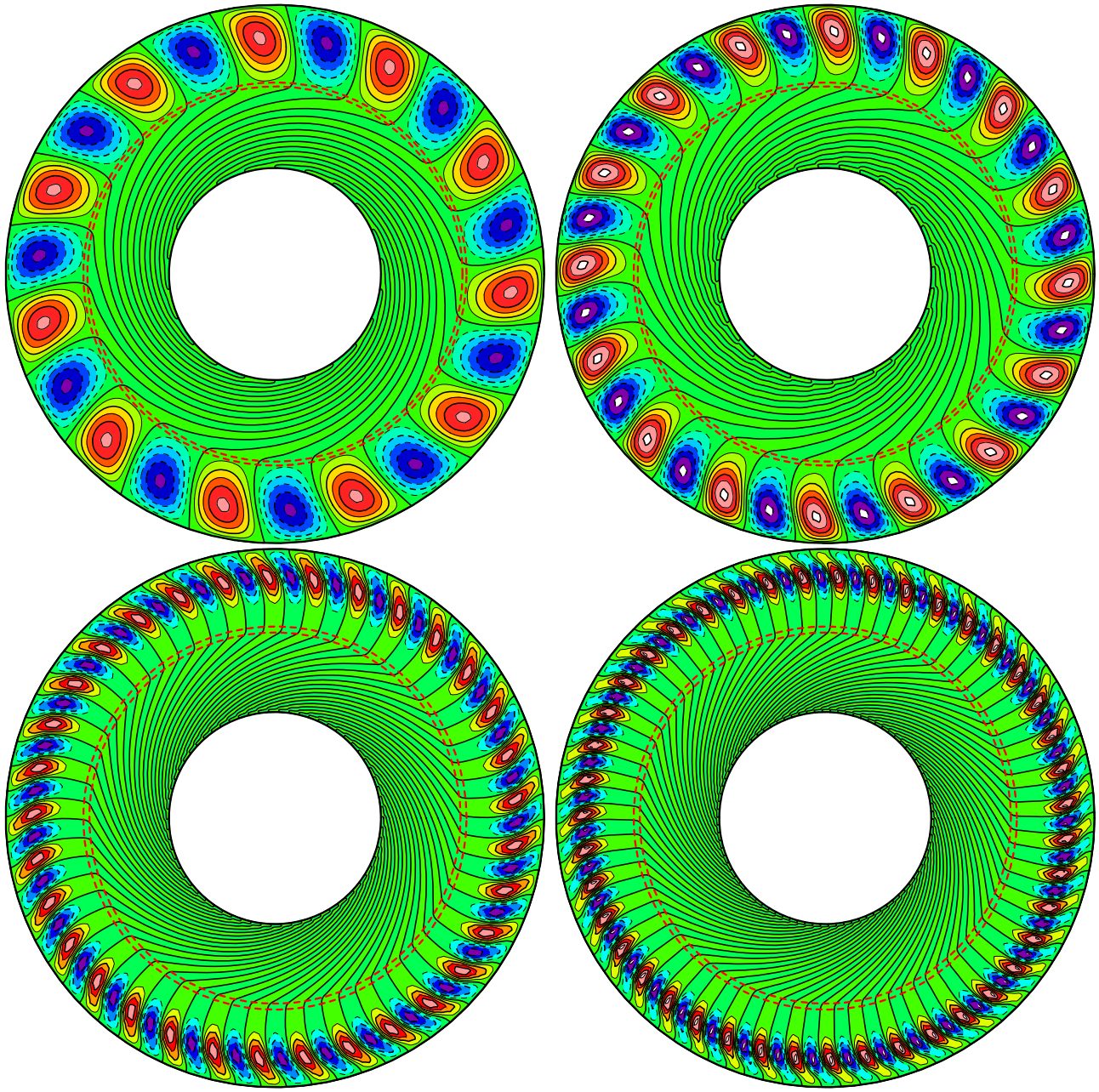

Figure 4. Radial velocity perturbations at the onset of convection for decreasing Ekman numbers (from 7.5×10^{-3} to 3×10^{-4}) for the M09 case series with $N_\rho^{cz} = 4.2$ and convective envelope aspect ratio $\beta^{cz} = 0.71$. Two red dotted lines indicate the bottom of the convection layer and boundary between the evanescent and wavy regions in the radiative layer.

Brun et al. (2017, see their Figure 4). The explanation for this large difference is as follows: in the linear stability analysis, the diffusive flux must carry the heat otherwise transported by the convective motions. In our setup, it is the spherically symmetric entropy flux that does so, the one proportional to κ_0 a very steep function of the radius r that peaks at the very surface. As a consequence, the nonlinear model has a large Nusselt number, with the enthalpy flux carrying all the stellar luminosity in the midlayers. When computing the linear stability state, this nonlinear enthalpy flux resulting from the correlation between temperature fluctuations and radial velocity perturbations does not exist. Only the diffusion flux is left to do the job of carrying the stellar luminosity outward, and this yields a very large entropy gradient.

4.2. Velocity and Entropy Patterns at Convection Onset

We now turn to analyzing the most-unstable convection modes that would be the first to be excited in all 15 cases. For this purpose, we display several equatorial slices of either the radial velocity or the entropy perturbation.

In Figure 4, we display for the M09 case series a contour plot of the radial velocity at the onset of convection for four different values of the Ekman number at fixed stratification N_ρ^{cz}. We indicate using a red dashed line the separation between the stably (below) and unstably (above) stratified layers in the simulated domain. We note the strikingly different patterns that results from our analysis and that could have been anticipated by looking at the change of m_c in Table 2. As we decrease the Ekman number, we see that the most-unstable mode becomes

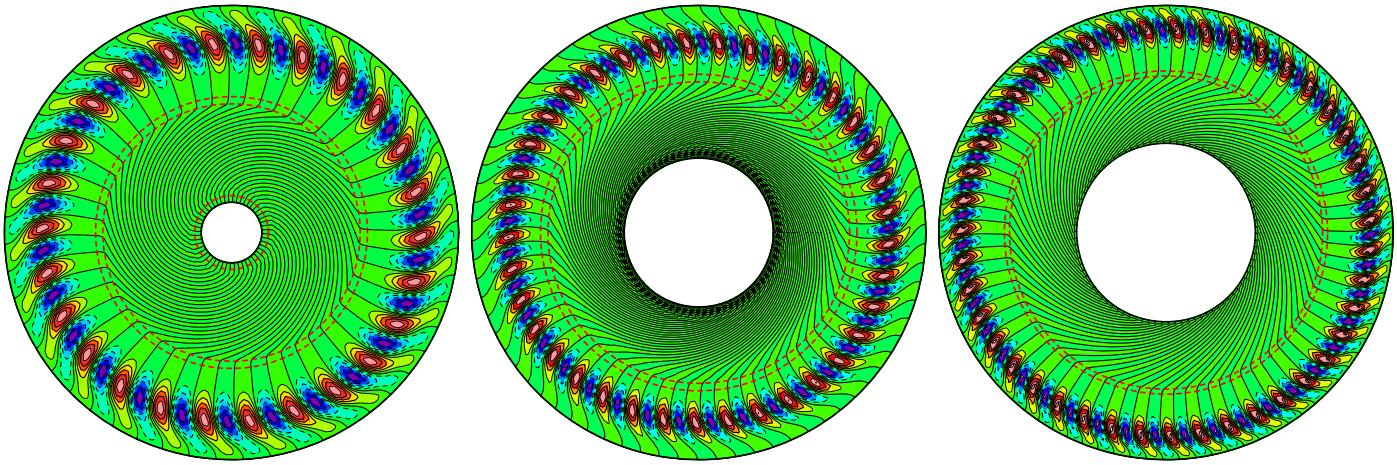

Figure 5. Radial velocity perturbations at the onset of convection for an Ekman number around 3×10^{-4} by varying N_ρ^{cz} from 3.7 to 4.2 along with the convective aspect ratio β^{cz} from 0.59 to 0.71. The cases with M05R1, M07R3, and M09R5 are shown from left to right. The two red dotted lines in the middle of the shell indicate the bottom of the convection layer and the boundary between the evanescent and wavy region in the radiative layer. Note that there exists another evanescent region in the innermost part of the M05R1 model, which is shown with the red dotted line.

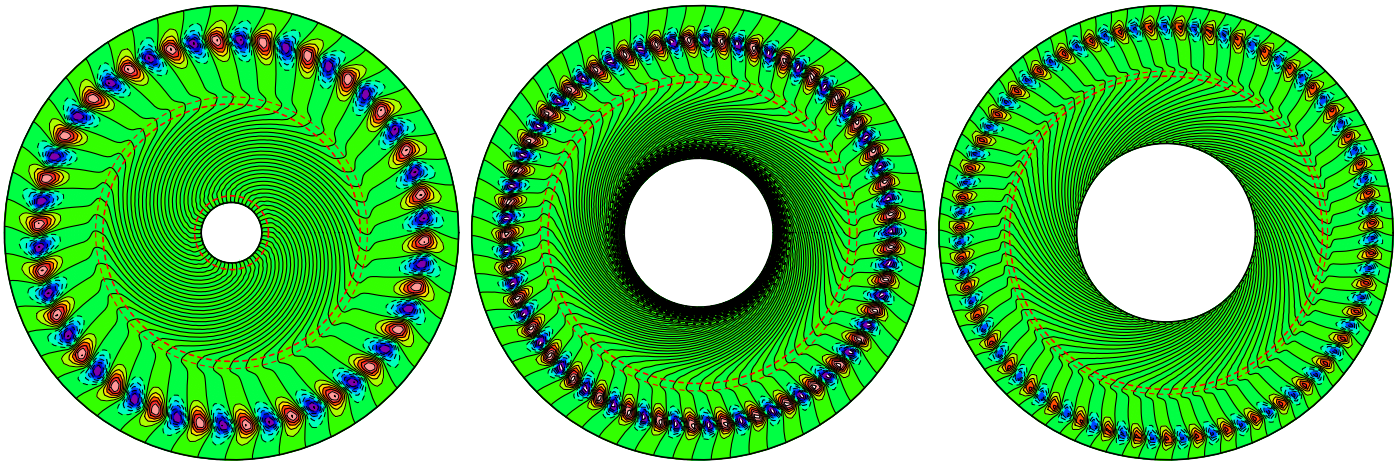

Figure 6. Companion figures to Figure 5 but showing the entropy perturbations at the onset of convection. Note the different tilt at the upper part of the domain. This is likely the consequence of the diffusion process acting dominantly in the upper part of the domain. As the convective structure moves in the prograde direction, the thermal diffusion of the entropy perturbation associated with the convective patterns moves radially outward with some time lag (proportional to the local frequency).

increasingly of smaller scale and that its radial extent also shrinks in size, becoming mostly confined to the top-middle part of the unstably stratified layer (see Figure 13 for the 1D radial cut that confirms this trend). It tends to locate itself where the entropy gradient is the most negative (see Figure 2). We also note the systematic prograde tilting of the patterns, which seems to be increasingly tilted as we go from the top-left to the bottom-right panels. Also note the distinctive spiraling pattern in the radiative (stably stratified) zone. This pattern is associated with internal gravity waves. We defer to the next section a discussion of their properties.

In Figure 5, in which we have selected three cases with approximately the same Ekman number $\sim 3 \times 10^{-4}$ we note a significant change of pattern, with much smaller features in the M09R5 case. The critical m_c value varies from 26 (left panel) to 43 (right panel; i.e., a 65% variation) for an otherwise relatively small change of N_ρ^{cz} (14%). This is likely due to the concurrent change by 20% of the convective aspect ratio β^{cz}. As both increase simultaneously from left to right, this leads to the observed increase of the critical m_c value, resulting in the much smaller convective velocity patterns in M09R5.

In the companion Figure 6, we display the entropy instead of the radial velocity for the same three cases as in Figure 5. The radial extent and location as well as the horizontal size of the entropy patterns clearly resemble those of the convective velocity discussed previously. As both the stratification and aspect ratio β^{cz} are increased, the convective (entropy) patterns shrink in size. However, there is one distinctive difference—the horizontal tilting of the patterns near the top of the domain. While with the velocity patterns, the patterns are prograde throughout the convectively unstable domain, the tilt of the entropy features changes sign near the surface. This is likely due to the fact that in that part of the domain diffusive processes dominate the balance, leading to a longitudinal lag as the convection mode propagates.

4.3. Scaling of Critical States

As discussed in the introduction, there is a long history of studies trying to assess how the onset of convection is influenced by various control parameters and physical configurations in geo- and astrophysical fluid dynamics. Moreover, generic scaling laws have been identified in some parameter

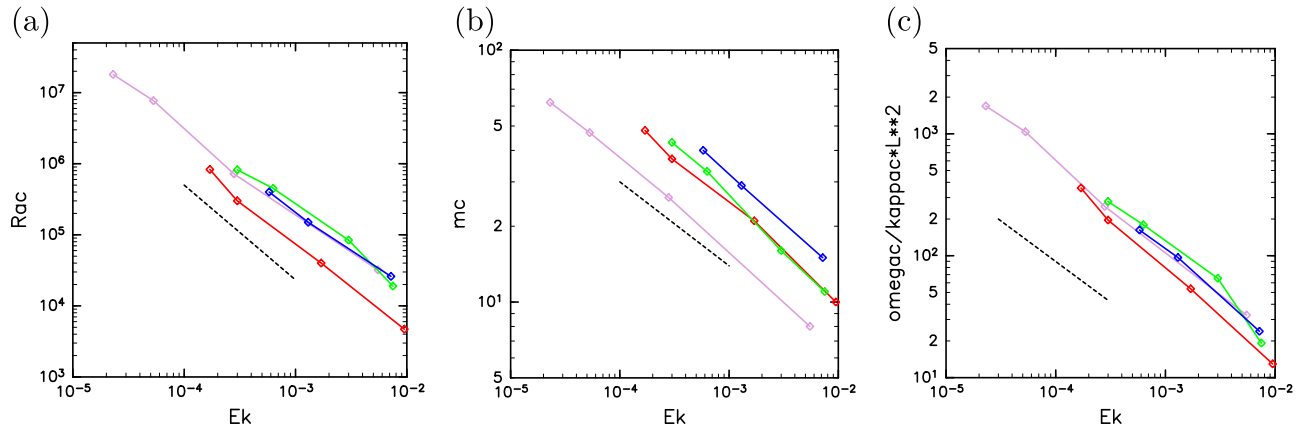

Figure 7. (a) The critical Rayleigh number as a function of the Ekman number. The dotted line is the slope with $-4/3$ power. (b) The critical azimuthal wavenumber as a function of the Ekman number. The dotted line is the slope with $-1/3$ power. (c) The nondimensional critical frequency ($\omega_c L^2/\kappa^{(c)}$) as a function of the Ekman number. The dotted line is the slope with $-2/3$ power. The magenta, red, green, and blue lines are for the M05, M07, M09, and M11 series, respectively.

regime. We wish here to compare our results to these previously published scaling laws. To this end, we plot in Figure 7 as a function of the Ekman number in a log–log plot the sensitivity to parameter change of m_c, ω_c, and Ra_c and compare this to the classical scaling (shown as a dotted line with the appropriate slope in each panel). In all three plots, we note a good overall agreement in the slopes (scaling law) achieved. This confirms that our stability analysis and results on the critical states are robust. To recover the appropriate scaling for ω_c, we need to represent a dimensionless frequency rather than the value directly quoted in Table 2. When dividing ω_c by the inverse of a diffusion timescale, we see that all 15 models collapse onto each other and follow the $-2/3$ scaling law, already identified in previous studies. For Ra_c and m_c, because these quantities are by essence without dimensions, we do not need to do the same. We see that they do follow very well the classical scaling with Ekman number. Ra_c is found to scale close to $E_k^{-4/3}$ and m_c to $E_k^{-1/3}$. We note a small departure from these Boussinesq scaling as can be expected with the high degree of stratification of our models.

Also note that in Figure 7, m_c is the most sensitive quantity with respect to the aspect ratio β^{cz} because of little overlap of the four lines contrary to the frequency ω_c.

5. Mean Flows

We now consider the mean flows established in each model by their respective most-unstable critical mode. To this end, we first present our set of second-order mean flow equations. Then, we discuss the resulting mean (longitudinally averaged) rotation profiles found in the computation domain using color contour plots in the meridional (r, θ) plane and the key physical mechanisms establishing these profiles. As we find that for some slowly rotating cases nonuniform rotation profiles are also established outside the unstable layer, we also discuss in some length the role of gravity waves in transporting angular momentum in the deep stable interior of these cases.

5.1. Equation for Second-order Analysis

Here, the calculation of the zonal mean steady meridional profile excited by critical convection is given. Zonal mean variables are denoted by $\langle(\cdot)\rangle$ and the second-order variables by $(\cdot)^{(2)}$. Then, each variable is expanded as follows:

$$\boldsymbol{u} = 0 + \boldsymbol{u}' + \boldsymbol{u}^{(2)}, \quad S = S_0 + S' + S^{(2)},$$
$$T = T_0 + T' + T^{(2)}, \quad p = p_0 + p' + p^{(2)}. \tag{17}$$

Substituting them into Equations (1)–(3), taking up to the second order of the disturbances, and performing a zonal average yield

$$\nabla \cdot (\overline{\rho}\langle \boldsymbol{u}^{(2)}\rangle) = 0, \tag{18}$$

$$-2\Omega \boldsymbol{k} \times \langle \boldsymbol{u}^{(2)}\rangle - \nabla\left(\frac{\langle p^{(2)}\rangle}{\overline{\rho}}\right) - \frac{\langle S^{(2)}\rangle}{C_p}\boldsymbol{g}(r) + \frac{1}{\overline{\rho}}\langle \boldsymbol{\mathcal{F}}_\nu^{(2)}\rangle = -\langle \boldsymbol{u}' \times \boldsymbol{\omega}'\rangle + \nabla\left(\frac{1}{2}\langle |\boldsymbol{u}'|^2\rangle\right), \tag{19}$$

$$-\overline{\rho}\overline{T}(\langle \boldsymbol{u}^{(2)}\rangle \cdot \nabla)(\overline{S} + S_0) + \nabla \cdot [\kappa_{\rm rad}\overline{\rho}C_p\nabla\langle T^{(2)}\rangle + \kappa\overline{\rho}\overline{T}\nabla\langle S^{(2)}\rangle] = \overline{\rho}\overline{T}\langle(\boldsymbol{u}' \cdot \nabla)S'\rangle - \langle Q_\nu'\rangle. \tag{20}$$

The left-hand sides consist of linear terms of second-order variables while the right-hand sides express the nonlinear effects of critical convection. Note that we can calculate the mean zonal field generated by each nonlinear effect separately as you can see below, as these equations are linear with respect to the second-order variables.

5.2. Mean Flow Profiles

We display in Figure 8 the 15 longitudinal velocity profiles obtained from our second-order mean flow analysis. The models are sorted from the slowest to the fastest rotating cases from left to right for each mass bin, with the lowest mass models, the M05 case series, being displayed on the top row and the heaviest, M11 case series, at the bottom row. The first important result is that none of the models show retrograde longitudinal profile around the equatorial surface; they all have a prograde differential rotation. This is in sharp contrast with the nonlinear calculations published in Brun et al. (2017), for which M05S, M07S, M09S, and M11R1 all exhibit retrograde angular velocities (see Figure 1 for an illustration of the antisolar rotation state). This means that the antisolar differential rotation profile found in the nonlinear models is due to the interactions of a broad range of modes of convection excited in the fully developed convection zone of these

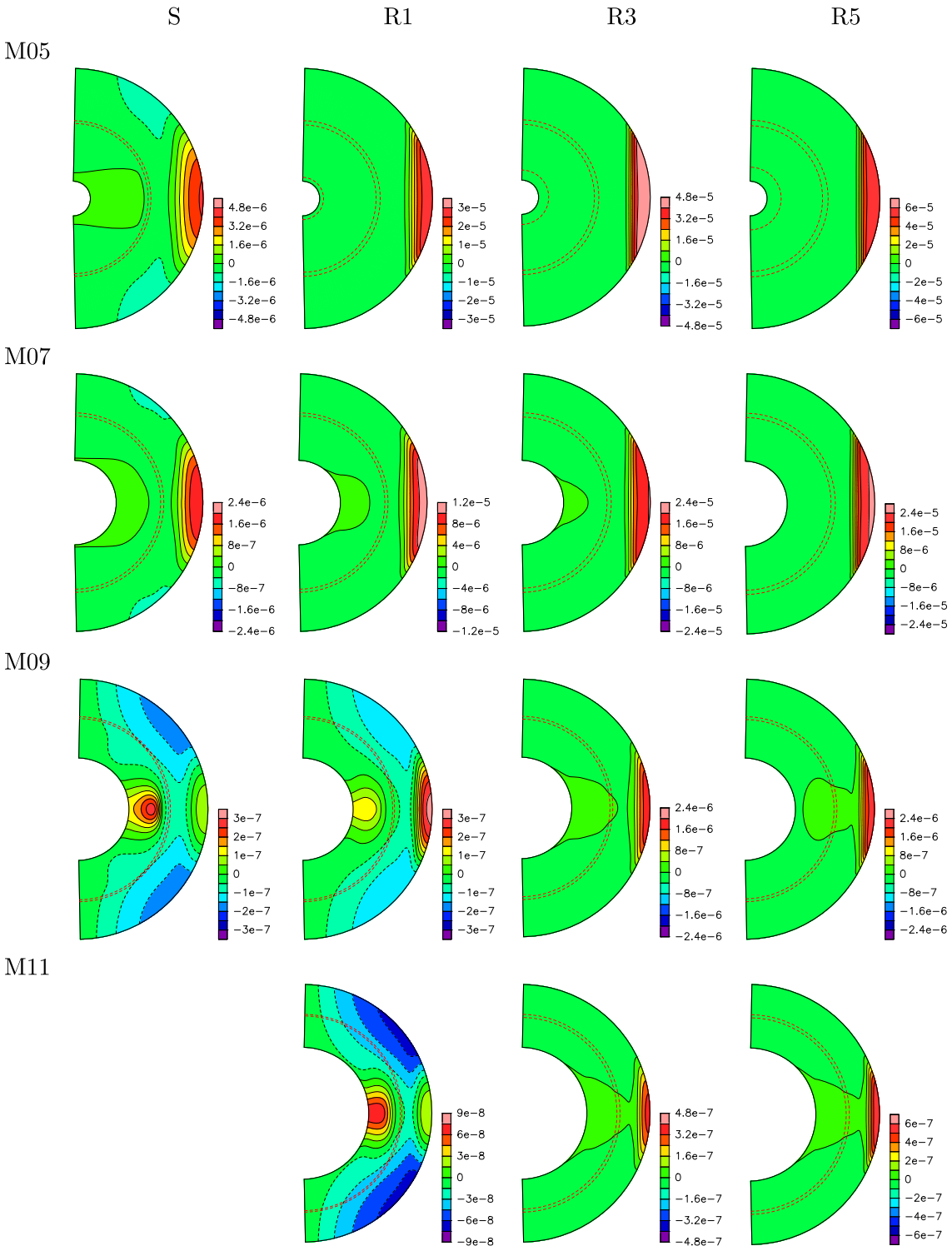

Figure 8. Mean zonal flows excited by critical convection evaluated with the weak nonlinear theory.

nonlinear cases. As we have seen in Table 2, all these slow-rotating models have a high level of supercriticality ($Ra/Ra_c > 60$), so their profile is the end result of complex convection mode interactions that lead to angular momentum transport that results in such an antisolar rotation state. Our study indicates that at the onset of convection, the slow-rotating models with large Rossby number do not have the same type of angular momentum transport and that only one mode is simply not enough to reach that antisolar state (in the parameter regime covered by our study, recall that for high Prandtl number cases, retrograde states were found by Takehiro & Hayashi 1999).

While all models at the onset of convection possess prograde longitudinal velocity, we do notice that the slowly rotating cases (those on the left-end side of the figure) do posses a peculiar meridional profile. Indeed, retrograde bands exist at midlatitude, and even more surprising, a prograde flow establishes itself in the equatorial region in the stably stratified interior. This is unexpected as our study focuses on the onset of

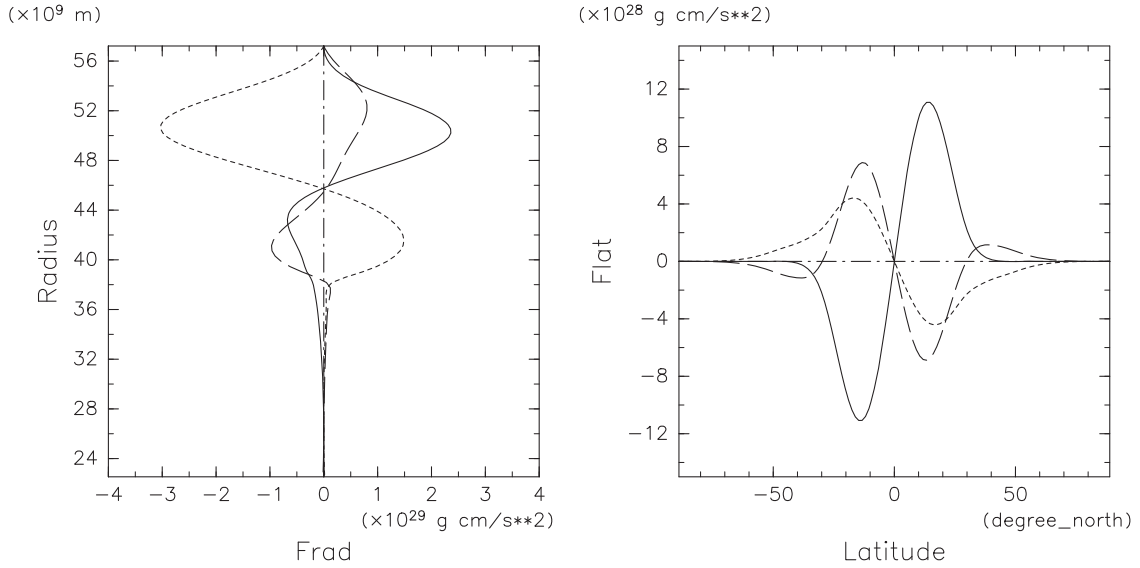

Figure 9. Radial and colatitudinal angular momentum fluxes of weak nonlinear solutions for the M09S case. The solid, broken, and dotted lines indicate the angular momentum fluxes due to Reynolds stress, the mean meridional circulation, and viscosity, respectively. Broken dotted lines indicate total angular momentum flux.

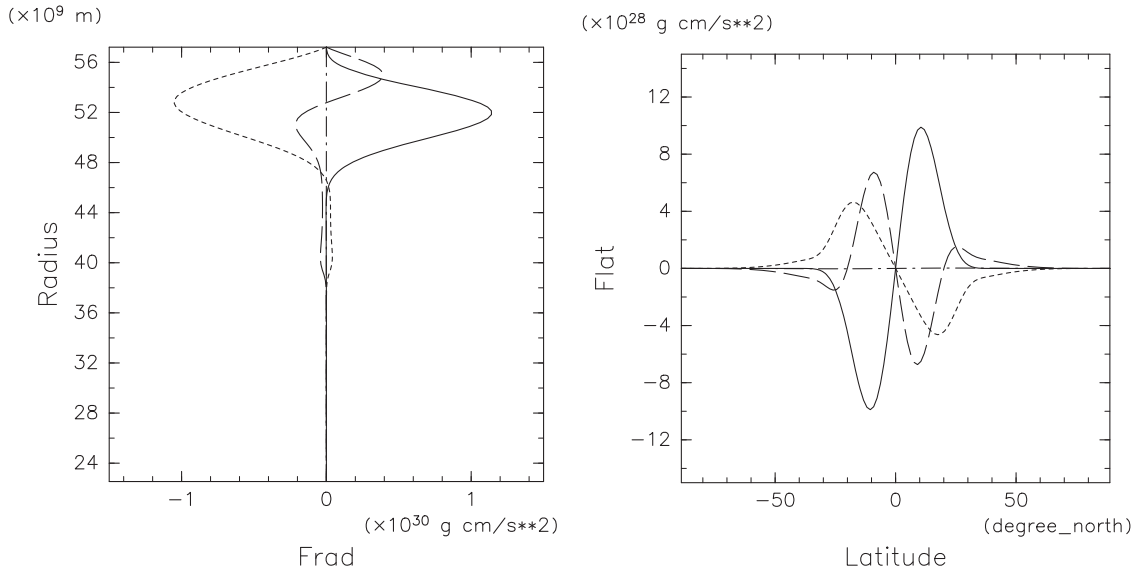

Figure 10. Radial and colatitudinal angular momentum fluxes of weak nonlinear solutions for the M09R3 case. The solid, broken, and dotted lines indicate angular momentum fluxes due to Reynolds stress, the mean meridional circulation, and viscosity, respectively. Broken dotted lines indicate total angular momentum flux.

convection in the unstably stratified external part of the domain, and the second-order mean flow analysis supposedly was expected to assess the angular momentum transport there as well. The fact that a non-solid-body rotation established itself outside the unstable layer is very interesting as it must be through a physical mechanism different from convection mode interaction. The likely source of angular momentum transport deep in this radiative layer must be the Reynolds stresses associated with gravity waves as we do not include magnetic effect in this study. Indeed, such waves can be guessed in the equatorial slices discussed in Section 4, that possess in their radiative interior the characteristic spiraling pattern of gravity waves (see, for instance, Alvan et al. 2014, 2015, and references therein). This is the first time that such a behavior is observed in linear stability analysis of convective flow and is the direct consequence of our choice of including in the analysis a stably stratified layer to improve the realism of the bottom boundary conditions. We defer to the next subsection a detailed discussion of the angular momentum transport realized in the stably stratified layer of the slow-rotating models where we provide some elements of internal gravity waves theory in stars.

For now, we wish to discuss the angular momentum balance achieved in the unstable convective upper layer. In Figures 9 and 10, we display the angular momentum balance of cases M09S and M09R3. Following Brun & Toomre (2002), we integrate in the latitude the radial component angular momentum flux and in the radius the colatitudinal component of the angular momentum flux. This allows us to assess the sense and amplitude of the transport of angular momentum within the computational domain. We further decomposed the fluxes into their Reynolds stresses (solid line), mean meridional circulation (dashed), and viscous (dotted) components. Turning first to the radial balance (left panels), we note that for case

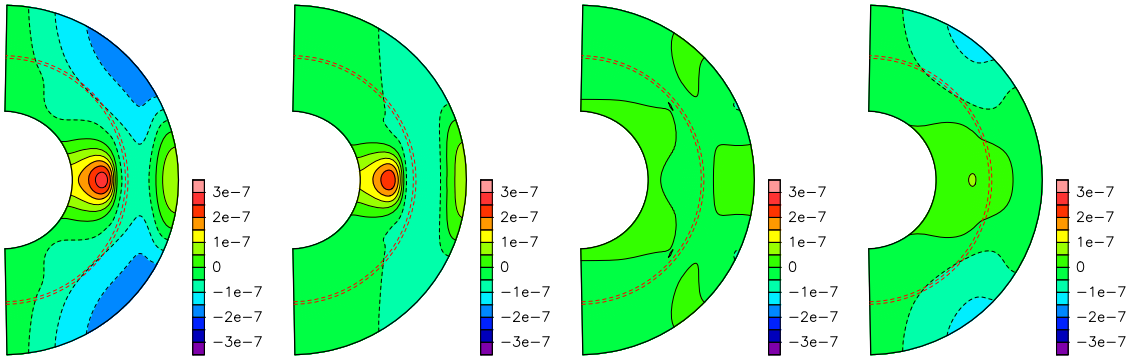

Figure 11. Mean zonal flow excited by each nonlinear term of the critical convection for the M09S case. (a) Total mean zonal flow. Mean zonal flow generated (b) by the nonlinear term of the toroidal equation, (c) by that of the poloidal equation, and (d) by that of the entropy equation.

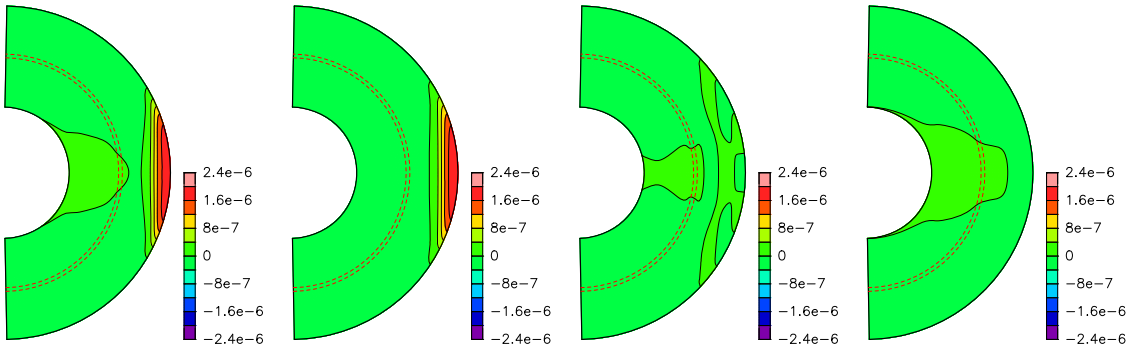

Figure 12. Mean zonal flow excited by each nonlinear term of the critical convection for the M09R3 case. (a) Total mean zonal flow. Mean zonal flow generated (b) by the nonlinear term of the toroidal equation, (c) by that of the poloidal equation, and (d) by that of the entropy equation.

M09S, the Reynolds stresses carry outward the angular momentum in the upper half of the domain, helped by the meridional circulation. In the lower part of the convection zone, extending somewhat into the radiative stably stratified layer, they reverse and transport the angular momentum downward. The viscous fluxes have opposite signs throughout the domain. The nonvanishing angular momentum term in the stable layer explains why M09S exhibits a differentially rotating stable layer. For case M09R3, the story is slightly different. The main balance is still between the Reynolds stresses and the viscous diffusion, but it is mostly concentrated in the upper part of the unstable layer. The transport is much weaker deeper down in the unstable layer, certainly because the most-unstable convective mode does not spread to the entire unstably stratified layer. Moreover, the meridional circulation contributes to both sides. In M09R3, there is also almost no angular momentum transport in the stable layer. This is consistent with case M09R3 having an almost perfectly rigid rotation in its stable layer. In both cases, the radial balance is well established as their sum is close to zero as indicated by the dashed–dotted line. For the latitudinal balance (right panels), both cases exhibit the same behavior. Reynolds stresses are found to be positive (negative) in the northern (southern) hemisphere, opposed by both viscous and meridional circulation. This means that Reynolds stresses transport angular momentum toward the equator. Because the differential rotation is prograde in all cases shown in Figure 8, it is expected that the viscous flux goes toward the pole in each hemisphere as they tend to erode any gradient of angular velocity. The meridional circulation direction is the result of the imbalance between Reynolds and viscous stresses in latitude, through the so-called gyroscopic pumping (McIntyre 1998, 2007; Brun et al. 2011). All other cases have similar behavior and are thus not shown for the sake of conciseness of the paper. Please note that in Brun et al. (2017), slow-rotating cases have latitudinal angular momentum due to Reynolds stresses in the opposite direction to what we found in this analysis. This is consistent with the fact that in the nonlinear simulation, retrograde differential rotation states are found. It seems that the $v_\theta v_\phi$ Reynolds stress plays a key role in establishing antisolar differential rotation.

To complement the angular momentum analysis, we display in Figures 11 and 12 the contribution to the differential rotation profiles achieved in M09S and M09R3 of the mean zonal flow generated by the nonlinear term of the toroidal equation, by that of the poloidal equation, and by that of the entropy equation (via meridional circulation driven by entropy latitudinal contrast). We see that for the slowly rotating case M09S, the nonlinear term of the toroidal equation is the source of the differential rotation in the stable layer and at the surface near the equator. The midlatitude retrograde (blue) features are due to the thermal contribution. The fact that the Reynolds stresses are the source of the feature seen in the stably stratified layer is further proof of the involvement of gravity waves to do so.

By contrast, there is almost a one-to-one correspondence between the case M09R3 mean zonal flow and the Reynolds stresses, with little contribution from the two other terms. Hence, Reynolds stresses associated with the critical convection mode are the source of the mean flow observed in these rapidly rotating (low Ekman) cases. Moreover, in these cases, there is no significant angular momentum transfer in their

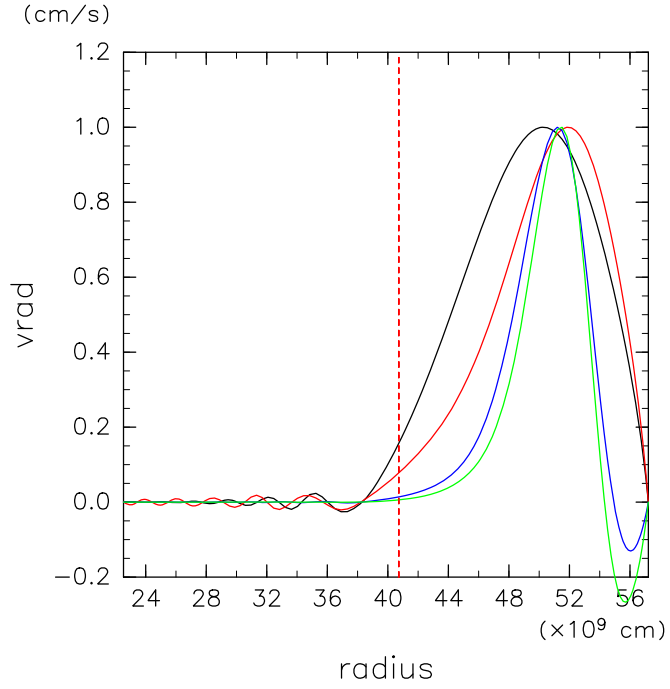

Figure 13. Structure of critical convection for the M09 series. Radial velocity profiles are shown. Black, red, blue, and green indicate the cases of M09S, M09R1, M09R3, and M09R5, respectively.

radiative interior even though they also exhibit spiraling patterns in the stably stratified layer when analyzing the equatorial slices of Figures 4 or 5.

We can understand that latter property by looking at the radial extent of the most-unstable convection mode. In Figure 13, we display for the four M09 cases a radial cut of the radial velocity in the equatorial plane at a given longitude (chosen such as to sample a local maximum for each case; please look again at Figure 4 for a contour plot of the radial velocity of the M09 case series). We see that the radial profile of the velocity changes significantly from one case to another. The model with the highest Ekman number (M09S) possesses a very broad profile, somewhat extending into the stable layer (delineated by the vertical red dashed line), its maximum peaking in the middle of the unstable layer. The M09R1 case also possesses a broad profile even if it is slightly narrower than case M09S. Both these cases exhibit wiggles in the stable layer, consistent with the presence of gravity waves that transport rather efficiently due to their relatively high-amplitude angular momentum in that layer (see below). By contrast, the other two models, M09R3 and M09R5, have narrow radial velocity profiles, with even a small negative value near the surface. The reason for the negative depth is that the patterns in the equatorial plane for these latter two cases are much more tilted and horizontally less extended, so a radial cut goes through more than one convective structure. At the base of the unstable layer, these models are also more damped with a tiny velocity amplitude. As a consequence, not much transport by gravity waves can be expected there as we will see in the next subsection.

5.3. Gravity Waves and Angular Momentum Transport in the Stable Layer

In this section, we wish to discuss how the slow-rotating cases, namely M05S, M07S, M09S, M09R1, and M11R1, establish their peculiar longitudinal velocity profile of non-solid-body rotation in the stably stratified deep layer. Recall that all these cases still possess a prograde differential rotation near the equator. The surprise comes from the fact that the second-order mean flow analysis reveals that these cases also develop a differential rotation profile elsewhere, other than in the outer unstable layer. The reason, as we have already mentioned, cannot be convection as it is confined in the upper part of the computational domain. It must be gravity waves excited by the critical convection mode of each slowly rotating case. Gravity waves are known to oscillate when their frequency is lower than the Brunt–Väisälä frequency (Pedlosky 1987). This is the case for most models in most of their radiative interior except for a small evanescent region near the base of the convection due to the sharp increase of N in that area. Indeed, when looking at the equatorial slices, all cases do display a spiraling pattern in their radiative interior. Note that the pitch angle of the spiral is determined by the ratio of ω_c/N and so changes in each model considered, as can be easily seen in Figures 4 and 5. One key question is: why do some cases develop non-solid-body rotation while others do not? In order to answer this question and understand the mechanism with which this critical frequency gravity-wave transport angular momentum, we need to look into gravity-wave angular momentum transport in stars (see, for more details, Ringot 1998; Talon et al. 2002; Rogers et al. 2013; Alvan et al. 2014, and references therein). What we wish to clarify is twofold:

(a) Why some cases have high-amplitude gravity waves in their radiative interior that lead to angular momentum transport and others do not, and
(b) Why, among the slowly rotating cases, the amplitude of the differential rotation in the stable layer differs, with for instance cases M05S and M07S displaying much less longitudinal velocity contrast compared to M09S, M09R1, and M11R1.

Let us start with the first question (a). It is clear from looking at Figure 8 that as we decrease the Ekman number from left to right, the transition occurs in the longitudinal and radial velocity profiles achieved in the simulation. Hence, there is clear influence of rotation on the existence or not of angular momentum transport in the radiative interior. We believe the reason is due to a change of convection structure with a decrease of the Ekman number. As shown in Figure 13, the convection patterns are significantly affected by the increase of the rotation rate and much less power reaches the base of the convection zone and thus the wave amplitudes are further reduced. This effect yields a much weaker gravity-wave signal in the stable layer for the R3 and R5 series of models. As a consequence, little or no angular momentum is being transported in the stably stratified zone of these models.

As a side comment, please also note that the respective critical frequencies ω_c of M05R3 and M05R5 are close to the maximum of N for these cases, so we expect an evanescent zone both near the top of the stably stratified domain and at the bottom. This is indeed what we observe in Figure 14 showing the Brunt–Väisälä frequency and ω_c for all four M05 cases.

As for the second question (point (b) above), we wish to understand why the slowly rotating cases M05S and M07S differ from their M09 and M11 equivalent. For this question, the previous argument on the radial extent of the critical convection mode does not hold here as all models have broad

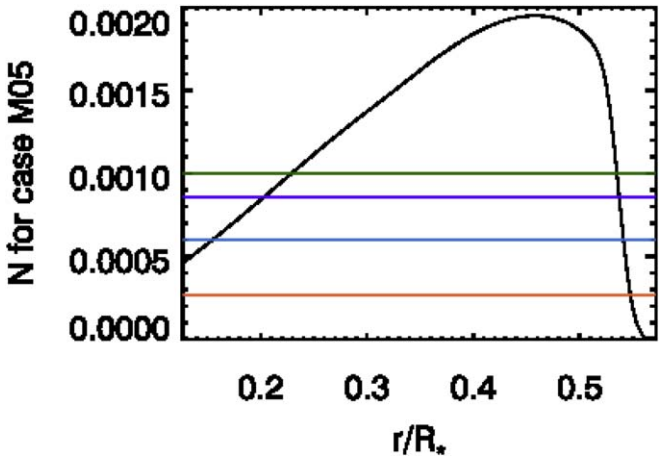

Figure 14. Brunt–Väisälä frequency for model series M05 and critical frequency from linear analysis. We note that waves excited at the critical frequency ω_c can propagate in almost the whole radiative zone, explaining why the spiraling patterns are visible in most of the inner stable region. All cases possess a shallow evanescent region at the base of their convective envelope. The M05 cases are special because they also possess an evanescent region near the bottom of the radiative stably stratified interior.

low-wavenumber convection patterns. The reason seems quite subtle and is likely linked to the way gravity waves are damped as they propagate in the radiative interior. As discussed in detail in Rogers et al. (2013) and Alvan et al. (2014), the wave amplitude is influenced by two phenomena: density stratification and thermal damping. Roughly speaking, $A \propto (A_0/\sqrt{\overline{\rho}})\exp(-\tau)$, with A_0 the amplitude of the wave at the base of the convection zone and τ the thermal radiative damping. As discussed in Rogers et al. (2013), the dependence of the wave amplitude on the background density as $\overline{\rho}^{-1/2}$ is linked to the conservation of the pseudo-momentum $\langle \overline{\rho} v_r v_\phi \rangle$, with $\langle\ \rangle$ representing a temporal and longitudinal average. Concerning the thermal radiative damping, this is explained in Zahn et al. (1997) and illustrated for a solar-like star in Alvan et al. (2015). The concept of thermal damping can be easily demonstrated through the following derivation.

We recall that the dispersion relation of internal gravity waves is

$$\omega^2 = \frac{N^2 k_H^2}{K^2}, \quad K^2 = k_H^2 + k_r^2, \tag{21}$$

where ω is the frequency of the wave, N is the Brunt–Väisälä frequency, and K, k_H, and k_r are total, horizontal, and radial wavenumbers. As we have already seen above, the group velocity in the radial direction is

$$C_{gr} \equiv \frac{\partial \omega}{\partial k_r} = -\frac{N k_H}{K^{3/2}} k_r = -\frac{\omega k_r}{K^2}. \tag{22}$$

Considering the following equation for wave propagation and viscous dissipation,

$$C_{gr}\frac{\partial \phi}{\partial r} = \nu \nabla^2 \phi \sim -\nu K^2 \phi, \tag{23}$$

and expressing the solution as follows:

$$\phi \sim e^{-\tau},\ \tau = \int_{r_c}^{r} \frac{\nu K^2}{C_{gr}} dr, \tag{24}$$

with τ a decaying factor, which is calculated as

$$\frac{\nu K^2}{C_{gr}} = \frac{\nu K^4}{\omega k_r}.$$

Here, when $N/\omega \gg 1$, k_r can be approximated as

$$k_r = \left(\frac{N^2}{\omega^2} - 1\right)^{1/2} k_H \sim \frac{N}{\omega} k_H.$$

Then,

$$\tau = \int_{r_c}^{r} \frac{\nu K^2}{C_{gr}} dr \sim \int_{r_c}^{r} k_H^3 \frac{N^3}{\omega^4} dr. \tag{25}$$

Equation (25) shows that the thermal damping depends on the horizontal wavenumber to the third power and on the ratio of the Brunt–Väisälä frequency to the third power with the wave frequency ω to the fourth power. Note that in our study of the critical state, ω will only take the value $\omega = \omega_c$, listed in Table 2.

In order to illustrate how the gravity waves are being damped in our slowly rotating cases we plot in Figures 15 for, respectively, M05S, M07S, M09S, M09R1, and M11R1 the thermal damping on the left panel and its product with the inverse of the square root of the background density. We note that for the first two cases, the damping is much stronger than for the other cases. We believe this explains why in cases M05S and M07S the gravity waves do not transport angular momentum as efficiently and as deep in the radiative layer as the other three cases.

By contrast, in Figure 16 we show the thermal damping (left panel) and its product with the inverse of the square root of the background density (right panel) for the M09 case series, and we clearly see that this cannot explain the difference in the radiative interior when the only parameter changed is rotation (or Ekman number). This confirms our finding for point (a) discussed above that what makes the difference for a given mass bin in the resulting mean flow deep in the stable layer is the extent of the convective pattern.

6. Discussion and Conclusion

In this work, we have studied if retrograde differential rotation states (slow equator, fast poles) can be found at the onset of convection instability. This is fundamental because such antisolar states have been found in many recent 3D nonlinear numerical simulations of rotating stellar convection, and we wish to know if such states could exist in real stars. We found that none of the linear critical states (see Figure 8) possess such a retrograde state. This means that only complex nonlinear mode interactions can generate such rotational states in the domain parameters we studied, and so given the high degree of turbulence in stars, this is likely going to happen also in stars. We mean that if diffusive retrograde rotation solutions at the onset of convective instability existed we could have argued that the nonlinear solutions were not supercritical enough and that the retrograde state was just a feature of mildly turbulent models. Finding the opposite is reassuring and gives an interesting observational perspective to look for such antisolar retrograde states in our cosmic neighborhood.

In order to perform this study and reach the above conclusion, we have performed a systematic analysis of the critical state of 15 stellar rotating convection simulations published recently in Brun

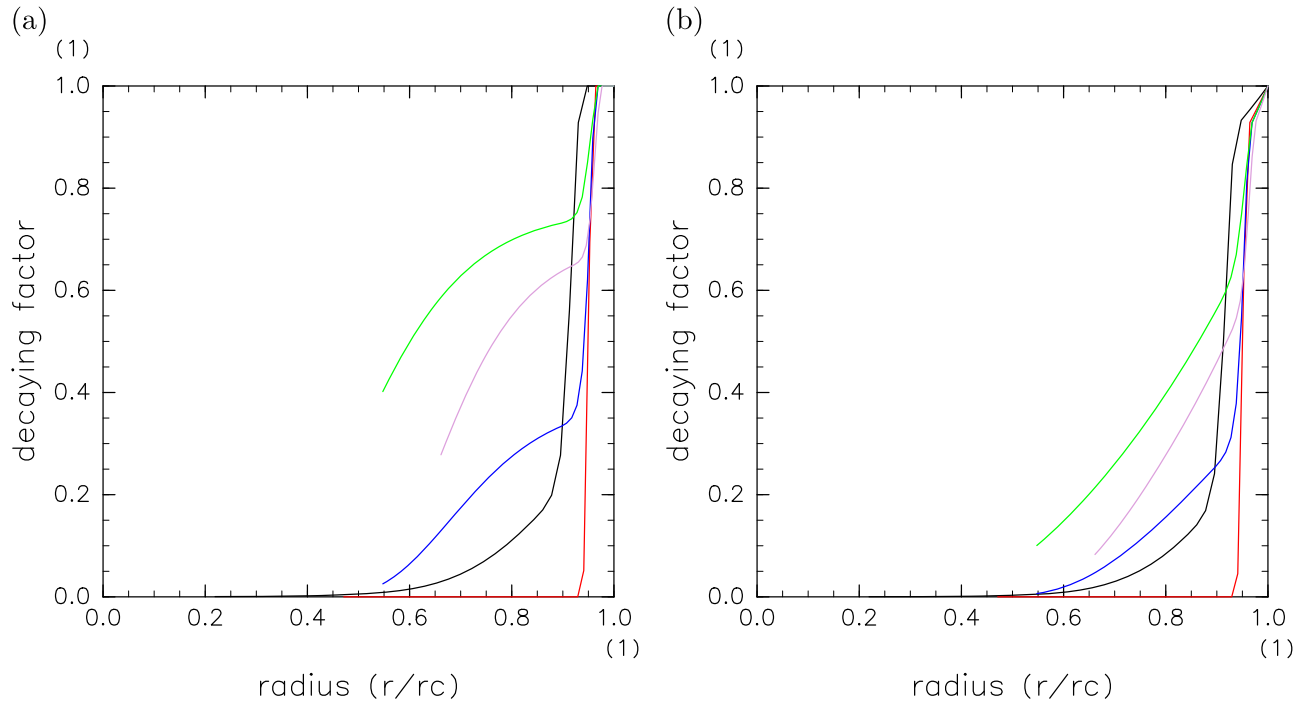

Figure 15. (a) Decaying factor $e^{-\tau}$ in the radiative layers. (b) Decaying factor $(1/\sqrt{\bar{\rho}})e^{-\tau}$ in the radiative layers. Black, red, blue, green, and magenta indicate the cases of M05S, M07S, M09S, M09R1, and M11R1, respectively.

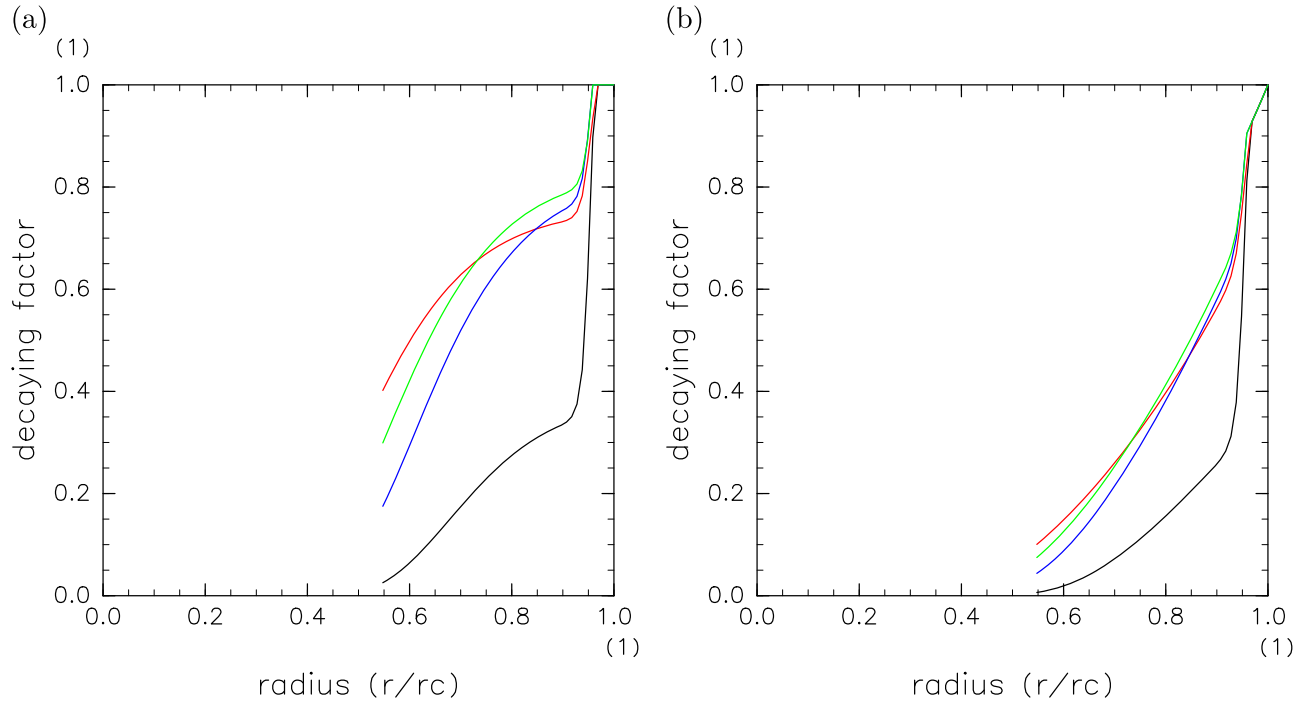

Figure 16. (a) Decaying factor $e^{-\tau}$ in the radiative layers. (b) Decaying factor $(1/\sqrt{\bar{\rho}})e^{-\tau}$ in the radiative layers. Black, red, blue, and green indicate the cases of M09S, M09R1, M09R3, and M09R5, respectively.

et al. (2017). We have computed through a linear perturbation analysis the most-unstable critical mode for each model in the anelastic approximation, characterized its critical wavenumber and frequency, and computed its degree of supercriticality by computing the associated critical Rayleigh number Ra_c (see Table 2). We have illustrated in equatorial slices how the critical modes evolve as a function of key parameters such as the Ekman number, number density scale height N_ρ^{cz}, and aspect ratio β^{cz}. We see that rotation strongly influences the mode structure, making it more confined both in longitude and radius. We find that the critical Rayleigh number can reach a very high value in excess of 10^6 for rapidly rotating highly stratified models. We have also recovered scaling law results published in the literature (Jones et al. 2009), such that, for instance, Ra_c scales as $E_k^{-4/3}$. Then, we computed the second-order mean flow response associated with the critical state. By analyzing this figure and

by noticing the absence of a retrograde rotation state, we reached the conclusion that antisolar retrograde states need complex nonlinear mode interaction to develop. We find that in all 15 cases studied, angular momentum is mostly transported by Reynolds stresses opposed by viscous transport. For the slowly rotating case, some contribution of the meridional circulation associated with temperature/entropy latitudinal contrast are also found. One key difference between the linear critical mode analysis simulations and the nonlinear turbulent solutions published in Brun et al. (2017) is the latitudinal transport of angular momentum by the $\langle v_\theta v_\phi \rangle$ term. For the slowly rotating cases (M05S, M07S, M09S, M11R1), in the nonlinear simulation they are poleward whereas for the linear analysis they are equatorward. This likely explains the reason why in the linear analysis the antisolar state is not found.

A specificity of our study is that it also includes a stably stratified layer below the surface unstable layer. This original setup has two important consequences. First, it improves the bottom boundary conditions by replacing an impenetrable wall with a more realistic coupling to a radiative interior. Second, to our own surprise, gravity waves can be excited in the whole radiative domain by the critical convection mode. This leads to interesting angular momentum redistribution, in particular for the slowly rotating (high Ekman number) cases. We find that the radial extent of the critical convection mode (see Figure 13) and azimuthal critical wavenumber both play a key role in determining if the Reynolds stress associated with the internal gravity waves will be large enough to make the stable layer depart from solid-body rotation. We also find that thermal damping and density stratification also explain why some slowly rotating (high Ekman number) cases display a stronger differential rotation in their stably stratified layer than other slowly rotating cases.

This study encourages us to compute even more turbulent simulations of rotating stellar convection at various Ekman and Rossby numbers in order to further delimit the regime where antisolar retrograde rotation states in stars could be found. In particular, this study focuses on Prandtl number (Pr) equal to $1/4$, and other studies have put forward the key role that Pr could have in the establishment of such prograde or retrograde states. Considering even lower values of Pr relevant for convection of solar-like stars would be interesting. Further, solar-like stars are magnetic, and it will be interesting to assess the role of Maxwell stresses in the resulting differential rotation profiles achieved as a function of Ro and E_k (see, for instance, Karak et al. 2015; Guerrero et al. 2016; Varela et al. 2016; Viviani et al. 2019) as well as the role of retrograde omega effect in stellar dynamo field generation (see Strugarek et al. 2018; Karak et al. 2020 for preliminary studies).

This work was supported by the Research Institute for Mathematical Sciences (RIMS), an International Joint Usage/Research Center located in Kyoto University. S.T. and M.Y. thank JSPS (Japan Society for Promotion of Science) KAKENHI Grant supports (15H05834, 17H02860, and 19H01947). A.S.B thanks Kyoto University and RIMS for their invitation during fall 2019 (and previous years) where most of this work was finished, the analysis performed, and the paper written. A.S.B. thanks CNES Solar Orbiter and PLATO grant support, INSU/PNST funding, as well as ERC STARS2 (207430) and Whole Sun (810218) grant support.

ORCID iDs

Shin-ichi Takehiro https://orcid.org/0000-0002-0857-3992
Allan Sacha Brun https://orcid.org/0000-0002-1729-8267

References

Alvan, L., Brun, A. S., & Mathis, S. 2014, A&A, 565, A42
Alvan, L., Strugarek, A., Brun, A. S., Mathis, S., & Garcia, R. A. 2015, A&A, 581, A112
Amard, L., Palacios, A., Charbonnel, C., et al. 2019, A&A, 631, A77
Brun, A. S., García, R. A., Houdek, G., Nandy, D., & Pinsonneault, M. 2015, SSRv, 196, 303
Brun, A. S., Miesch, M. S., & Toomre, J. 2011, ApJ, 742, 79
Brun, A. S., & Rempel, M. 2009, SSRv, 144, 151
Brun, A. S., Strugarek, A., Varela, J., et al. 2017, ApJ, 836, 192
Brun, A. S., & Toomre, J. 2002, ApJ, 570, 865
Busse, F. H. 1970, JFM, 44, 441
Chandrasekhar, S. 1961, Hydrodynamic and Hydromagnetic Stability (Oxford: Clarendon)
Dormy, E., Soward, A. M., Jones, C. A., Jault, D., & Cardin, P. 2004, JFM, 501, 43
Gastine, T., Yadav, R. K., Morin, J., Reiners, A., & Wicht, J. 2014, MNRAS, 438, L76
Gilman, P. A. 1975, JAtS, 32, 1331
Gilman, P. A. 1977, GApFD, 8, 93
Guerrero, G., Smolarkiewicz, P. K., de Gouveia Dal Pino, E. M., Kosovichev, A. G., & Mansour, N. N. 2016, ApJ, 819, 104
Guerrero, G., Smolarkiewicz, P. K., Kosovichev, A. G., & Mansour, N. N. 2013, ApJ, 779, 176
Jones, C. A., Boronski, P., Brun, A. S., et al. 2011, Icar, 216, 120
Jones, C. A., Kuzanyan, K. M., & Mitchell, R. H. 2009, JFM, 634, 291
Karak, B. B., Käpylä, P. J., Käpylä, M. J., et al. 2015, A&A, 576, A26
Karak, B. B., Tomar, A., & Vashishth, V. 2020, MNRAS, 491, 3155
Landin, N. R., Mendes, L. T. S., & Vaz, L. P. R. 2010, A&A, 510, A46
Matt, S. P., Do Cao, O., Brown, B. P., & Brun, A. S. 2011, AN, 332, 897
McIntyre, M. E. 1998, PThPS, 130, 137
McIntyre, M. E. 2007, in The Solar Tachocline, ed. D. W. Hughes, R. Rosner, & N. O. Weiss (Cambridge: Cambridge Univ. Press), 183
Pedlosky, J. 1987, Geophysical Fluid Dynamics (Berlin: Springer)
Réville, V., Brun, A. S., Strugarek, A., et al. 2015, ApJ, 814, 99
Ringot, O. 1998, A&A, 335, L89
Roberts, P. H. 1968, RSPTA, 263, 93
Rogers, T. M., Lin, D. N. C., McElwaine, J. N., & Lau, H. H. B. 2013, ApJ, 772, 21
Sasaki, Y., ichi Takehiro, S., Ishiwatari, M., & Yamada, M. 2018, PEPI, 276, 36
Strugarek, A., Beaudoin, P., Charbonneau, P., & Brun, A. S. 2018, ApJ, 863, 35
Takehiro, S.-I., & Hayashi, Y.-Y. 1999, GApFD, 90, 43
Talon, S., Kumar, P., & Zahn, J.-P. 2002, ApJL, 574, L175
Varela, J., Strugarek, A., & Brun, A. S. 2016, AdSpR, 58, 1507
Vidotto, A. A., Donati, J.-F., Jardine, M., et al. 2016, MNRAS, 455, L52
Viviani, M., Käpylä, M. J., Warnecke, J., Käpylä, P. J., & Rheinhardt, M. 2019, ApJ, 886, 21
Wang, J., Miesch, M. S., & Liang, C. 2016, ApJ, 830, 45
Zahn, J. P., Talon, S., & Matias, J. 1997, A&A, 322, 320
Zorec, J., Rieutord, M., Espinosa Lara, F., et al. 2017, A&A, 606, A32